CO2 degassing in the mantle triggers deep earthquakes at the Mid-Atlantic Ridge

Zhiteng Yu (zyu@ipgp.fr)
Geo-Ocean UMR6538
Satish Singh
Universite Paris Cite https://orcid.org/0000-0002-4594-801X
Léa Grenet
Geo-Ocean UMR6538
Marcia Maia
CNRS
Cédric Hamelin
Department of Earth Science, University of Bergen
Anne Briais
Geo-Ocean UMR6538
Lorenzo Petracchini
Istituto di Geologia Ambientale e Geoingegneria-Consiglio Nazionale delle Ricerche
Daniele Brunelli
Università di Modena e Reggio Emilia https://orcid.org/0000-0003-4839-1939

Article

Keywords:

Posted Date: September 20th, 2022

DOI: https://doi.org/10.21203/rs.3.rs-1945608/v1

CO_2 degassing in the mantle triggers deep earthquakes at the Mid-Atlantic Ridge

Zhiteng Yu[1*], Satish C. Singh[2*], Léa Grenet[1], Marcia Maia[1], Cédric Hamelin[3], Anne Briais[1], Lorenzo Petracchini[4], Daniele Brunelli[5,6]

[1]Geo-Ocean UMR6538, CNRS-Ifremer-UBO-UBS; Plouzané, 29280, France
[2]Université Paris Cité, Institut de Physique du Globe de Paris, CNRS; Paris, France
[3]Department of Earth Science, University of Bergen; Bergen, Norway
[4]Istituto di Geologia Ambientale e Geoingegneria-Consiglio Nazionale delle Ricerche; Roma, Italy
[5]Università di Modena e Reggio Emilia; Modena, Italy
[6]Institute for Marine Sciences ISMAR-CNR; Venezia, Italy

*Corresponding author: Zhiteng Yu (zhitengyu@gmail.com); Satish Singh (singh@ipgp.fr)

Present address: Zhiteng Yu, Geo-Ocean UMR6538, 29280, Plouzané, France.

Oceanic crust is formed by melt derived from the mantle at oceanic spreading centers. A small amount of melting initiates at about 150-300 km depths in the presence of volatiles (CO_2, H_2O)[1–3], but the extensive dry melting commences at 60-70 km depths due to the upwelling of the mantle as two diverging plates move apart[4,5]. However, how these melts migrate to the surface and what happens to these melts in the upper part of the mantle are still not understood. Using seismological data recorded by ocean-bottom seismometers, here we report the presence of deep earthquakes at 10-20 km depth in the hot mantle along the Mid-Atlantic Ridge axis, much below the brittle-ductile boundary, suggesting that these earthquakes are caused by a volume change associated with the CO_2 degassing from the ascending melt. The geochemical analyses of basalts from the ridge axis show an abnormally high quantity of CO_2 (>1.9 wt%) in the primitive melt, confirming the CO_2 degassing hypothesis. The large concentration of CO_2 in the primitive melt will influence the presence of melt beneath the lithosphere-asthenosphere boundary at sub-solidus temperatures.

At fast- and intermediate-spreading ridges, axial melt lenses (AMLs) are commonly used to separate the brittle lithosphere above partially molten crust and mantle below[6], and define the brittle-ductile boundary (BDB). However, at slow- and ultraslow-spreading ridges, in the absence of images of AML, the maximum depth of earthquakes, corresponding to the 700±100°C isotherms[6–8], is used to define the BDB. Based on thermal models, earthquakes are expected to occur at depths <8 km below the seafloor (bsf) beneath slow-spreading ridges and at depths <12 km bsf beneath ultraslow-spreading ridges[9]. However, some deeper earthquakes have recently been observed beneath slow- and ultraslow-spreading ridges[10–12] that have been associated with either deep-rooted detachment faults[10,11] or cold thermal regimes caused by deep fluid circulation[12]. Deeper earthquakes have also been observed along oceanic transform faults (TFs), which have been interpreted to be due to the semi-brittle deformation in high-temperature (HT) hydrated mylonite shear zones[13,14]. These observations indicate that the maximum depth of earthquakes also depends on other factors such as tectonic, hydrothermal, and petrological processes.

Here, we present the results of a seismicity study from the Mid-Atlantic Ridge (MAR) in the equatorial Atlantic Ocean (Fig. 1a). The MAR here spreads at a half spreading rate of 16 mm/yr[15]. The seismicity data were acquired using 19 ocean-bottom seismometers (OBSs) during the SMARTIES cruise[16] (Fig. 1b). The study area is located in the northern part of the ~200-km-long MAR segment between the Romanche and Chain TFs, in the vicinity of the eastern Romanche ridge-transform intersection (RTI) (Fig. 1A). The studied portion of the ridge is ~120 km long, which is offset by non-transform discontinuities (NTD) (Fig. 1b). The ridge can be subdivided into four 20-50-km-long sub-segments (Fig. 1b): the RTI section, the first NTD (NTD1), a short central ridge segment (MAR), and the second NTD (NTD2) (Figs. 1 and 2). The RTI sub-segment seems to have been formed by a westward dipping detachment fault with a prominent oceanic core complex (OCC) on the east (Fig. 2a). The extensive observation of peridotites on the seafloor[16,17] (Fig. 1b) indicates the presence of exhumed mantle and supports the tectonic origin of this sub-segment. The surface of this OCC is heavily cut by N201°E- and N22°E-striking normal faults, suggestive of recent active tectonic deformation (Fig. 2a). The NTD1 is ~50 km long and oriented at N76°E and has a large number of N118°E-striking normal faults (Fig. 2a, c). The presence of both pillow basalts and peridotites on the seafloor (Fig. 1b)[16,17] indicates its mixed tectonic and magmatic origin. The MAR central segment south of NTD1 is ~22 km long, with a typical 10-km-wide median valley and an N154°E-oriented neo-volcanic ridge at the center (Fig. 2c), suggestive of a magmatically robust segment, which is further supported by the extensive observation of basalts on the seafloor (Fig. 1b)[16]. The NTD2 is ~33 km long, orientated at N110°E, with large areas affected by a complex pattern of normal faults, striking at N115°E and N145°E (Fig. 2e).

The hypocentre locations along each sub-segments are shown in Fig. 2, and all determined earthquakes are shown in Extended Data Fig. 1 (Methods). There are three key observations along these four sub-segments: (1) the majority of shallow earthquakes (0-6 km) occur on the outside corner of the RTI beneath the OCC surface as well as on the west off-axis region of the MAR; (2) the deep seismicity (~10-20 km) lies beneath the MAR axis; (3) earthquakes at normal depths (4-10 km) occur beneath the southern NTD2 (Fig. 2, Extended Data Fig. 1).

For a full spreading rate of ~32 mm/yr[15], the depth of the AML would be ~7 km, and the maximum earthquake depth should not exceed 10 km (Extended Data Fig. 2, Supplementary Table 1), corresponding to a thickness of the brittle lithosphere <10 km. This depth range is only observed beneath the OCC (<6 km, Fig. 2b) and NTD2 (<10 km, Fig. 2f). The absence of deep seismicity west of the OCC (Fig. 2a), which is expected beneath the axial valley or at the hanging wall side of the detachment fault[10], suggests that this detachment fault is inactive. However, the shallow earthquakes directly beneath the OCC and the presence of high-angle normal faults cutting the OCC surface suggest that the ridge axis has moved eastward beneath the OCC[17]. Beneath the NTD2, the earthquakes are slightly deeper, down to ~10 km (Figs. 2e, f), which is expected for a slow-slipping NTD (Extended Data Fig. 2, Supplementary Table 1). These results suggest that the brittle lithosphere is at most ~10 km thick at the segment boundaries.

The BDB should become shallower southward as we move away from the RTI because the cold-edge effect of the 45-Ma-old lithosphere would decrease southward[17–19]. However, we observe deep earthquakes (16-19 km) along the MAR central segment axis (Figs. 2c, d), the deepest earthquakes documented to date at slow-spreading centers (Extended Data Fig. 2). Seismic refraction studies indicate that the western 8-Ma-old crust is 5.4±0.3 km thick[20], suggesting that these earthquakes mostly occur in the mantle below 10 km depth, with some scattered events in the crust (Fig. 2d), far exceeding the suggested maximum depth range (Extended Data Fig. 2). An earthquake cluster is also found on the west side of the axial valley, with shallow focal depths (~2-6 km) (Fig. 2d), suggesting that the deep events are real, not an artifact of location errors. The depth resolution tests (Methods) further support that these events are indeed deep.

One could interpret these deep earthquakes beneath the MAR as a result of an extremely cold and thick lithosphere, where the BDB corresponding to the 600-800°C isotherms[6–8] would be at ~20 km depth, similar to what was proposed for the Southwest Indian Ridge (SWIR) and Gakkel Ridge (GR)[12]. However, all the other observations are inconsistent with this interpretation. For example, the presence of hummocky morphology, volcanic cones, and a well-defined neo-volcanic ridge in the axial valley (Fig. 2c) indicates that the ridge segment is magmatic, unlike the smooth morphology related to the amagmatic spreading processes at the SWIR [21]. The seafloor across the ridge axis is characterized by bathymetric highs mostly cut by ridge-parallel normal faults (Fig. 2c), showing basaltic constructions supported by rock samples on the seafloor (Fig. 1b). In addition, the off-axis shallow seismicity (down to 6 km) west of the ridge axis (cross-section dd’, Figs. 2c, d) indicates that the BDB remains shallow (<10 km depth) up to ~1.3 Ma [22] in the vicinity of the MAR (Fig. 2c). Furthermore, the seismicity down to 10 km beneath the NTD2 reveals that the BDB is indeed at ~10 km (Figs. 2f), much shallower than the deep seismicity observed beneath the MAR. The thermal modeling [19] suggests that the temperature should be 1100-1200°C at 10-20 km depth (Fig. 3), and hence the mantle beneath the MAR axis is hot, as expected for a typical magmatic segment, not cold.

Hydrothermal circulations, however, could cool the lithosphere rapidly away from the ridge axis[23], deepening the seismicity and hence the BDB (Extended Data Fig. 2). Indeed, an extinct hydrothermal area is observed on the eastern flank of the NTD1[16] but is relatively far from the present axial valley (Fig. 2c), and hence would not affect the lithosphere beneath the ridge axis. Taken together, these results indicate that magmatism dominates the crustal accretion process at this MAR segment, and these earthquakes occur in a hot mantle at temperatures >1100°C (Fig. 3).

The presence of deep earthquakes at high temperatures in the mantle along TFs has been explained by the development of a localized high strain[24] in the semi-brittle HT mylonite shear zones[13,14]. Although a localized high-strain shear zone in the deep mantle beneath spreading centers can be expected to occur during the development of detachment faults[10,11], producing deep seismicity, the 10-km-wide axial valley is bounded by high-angle NNW-SSE oriented in-ward dipping faults (Fig. 2c), and does not show any evidence for the presence of a detachment fault. Some detachment faults and corrugated surfaces are observed 20-30 km west of the MAR, but there we observe shallow rather than deep seismicity (Fig. 2c), indicating that they are probably inactive now.

The third possibility is that these deep earthquakes in the mantle are associated with magmato-tectonic activities, similar to those observed in Askja, Iceland (depths >10 km)[25–27] and offshore Mayotte Island, in the western Indian Ocean (depths >30 km)[28]. The melt movement at depth could introduce high strain rates, producing brittle failure in the ductile lower crust[25,27]. Furthermore, pre-existing faults/fractures above a deep magma reservoir can activate the melt migration[28], producing earthquakes. However, the seismicity in Iceland occurs in the thickened crust[25,27], whereas, in the case of Mayotte, it occurs in a cold lithosphere[28]. In our case, although the off-axis shallow seismicity (<10 km) west of the ridge axis (Fig. 2c, d) might be related to the westward melt migration to a shallow depth at the crustal level, the deep seismicity occurs beneath the ridge axis in a hot mantle.

The fourth possibility is that the observed deep seismicity beneath the MAR is related to the CO_2 degassing from the ascending magma melt, causing a volume change, which in the presence of extensional stresses[29,30] could produce locally high strain rates to trigger deep earthquakes in the mantle (Fig. 3). As the solubility of CO_2 in silicate (dry) melts is strongly dependent on the pressure[31], nearly all the CO_2 in basalts erupted on the seafloor under hydrostatic pressures are generally degassed (80-90% loss)[31]. We would like to mention that the degassed CO_2 would remain in the liquid phase under high pressures. Given that an increase in pore pressure of only 2-3 bars can trigger earthquakes[32], we suggest the small pressure increase by the CO_2 degassing from the ascending melt should be capable of inducing earthquakes we observe beneath the ridge axis[29,30].

The primary concentration of CO_2 in mid-ocean ridge basalts (MORB) can be estimated using nonvolatile elements, such as Barium (Ba), Niobium (Nb), and Rubidium (Rb)[33–37]. Undegassed MORBs and MORB melt inclusions define global trends in the ratios of volatile to nonvolatile incompatible elements, such as CO_2/Ba

(81.3 ± 23)[35], CO_2/Nb (515 ± 112)[33], and CO_2/Rb (991 ± 129)[35] (Methods). Constraints on the pre-eruptive CO_2 content for degassed MORB can thus be obtained by examining their Ba, Nb, and Rb concentrations (Fig. 4a-c). We present a geochemical analysis of two new MORB samples (Methods) and one published sample[38], all collected along our central MAR segment (see locations in Fig. 1b). Although they have experienced a limited amount of fractional crystallization (Mg# > 70%)[35], they exhibit a high concentration of incompatible elements: Ba > 300 ppm, Nb > 40 ppm, and Rb >19 ppm (Fig. 4a-c). Comparing these values to the global data indicates that CO_2 concentration in the primary magma is very high, varying between 1.9 wt% and 4.8 wt% (Fig. 4).

Using the CO_2 solubility model[39], those melts (>1.9 wt% CO_2) would become saturated with CO_2 at ~1.5 GPa (~50 km depth) and 1300°C, and start CO_2 degassing at much deeper depths. However, no earthquakes are observed at depths >20 km beneath the MAR axis (Fig. 2d), which could be due to much higher temperatures (>1200°C) at 20-50 km depths[19] (Fig. 3) that would hinder the nucleation of earthquakes. As the melt migrates towards the surface, it would continue to degas, producing earthquakes between 10 km and 20 km depth range in the mantle.

If we assume that the volume change caused by the CO_2 degassing represents the fault size of earthquakes, we find that the volume change is of the order of ~0.5-2.1% (Methods), similar to the estimation derived from geochemical data. Based on our model (Fig. 3), at some ultraslow-spreading ridges (e.g., SWIR and GR) where deep mantle earthquakes have been observed[12], the CO_2 content is likely to be high. Previously, the highest amount of CO_2 for the melt has been reported at the SWIR (1.9 wt%)[35]. Between 5°S and 5°N in the equatorial Atlantic Ocean, previous studies[35,36] have suggested that the CO_2 segmented concentrations are generally high, reaching an average of ~2800 ppm and up to ~8799 ppm based on the CO_2/Rb and CO_2/Ba estimations[35], which has been attributed to recycled subduction zone components [34]. The degassed CO_2 from the melt at slow- and ultraslow-spreading ridges would react with the mantle rocks to produce CO_2-rich fluid inclusions that would migrate through the crust and reach the ocean floor and might contribute to the global CO_2 budget in the ocean and atmosphere[35].

Keller et al.[40] have shown that the presence of volatiles in the ascending melt does not only focus melt beneath the ridge axis but the melt is also flushed away from the ridge axis and may reside at the lithosphere-asthenosphere boundary (LAB). Recent studies from the equatorial Atlantic region[41,42] show the presence of melt at sub-solidus temperatures (~1250° C) at the LAB, requiring the existence of volatile that would reduce the solidus temperature. To explain the reflections at the LAB, Audhkhasi and Singh (2022)[41] proposed that ~1.1 % of melt is required at the base of the LAB, with the water content up to 332 ppm. Our discovery of a large amount of CO_2 in the melt suggests that the depressed solidus may be attributed to volatiles from a combination of CO_2 and H_2O[40], which would also extend the depth of incipient wet melting beneath spreading centers[1,3]. The presence of seismicity at 10-20 km depth suggests that ascending melt resides in the mantle at these depths, fractionates, and evolves[4] before moving upwards forming the oceanic crust. The melt could also freeze at the base of the lithosphere, producing sub-horizontal reflections as observed beneath the young Juan du Fuca plate[23], and leading to high compositional heterogeneities in the oceanic lithosphere[23,40].

References

1. Dasgupta, R. *et al.* Carbon-dioxide-rich silicate melt in the Earth's upper mantle. *Nature* **493**, 211–215 (2013).
2. Dasgupta, R. & Hirschmann, M. M. Melting in the Earth's deep upper mantle caused by carbon dioxide. *Nature* **440**, 659–662 (2006).
3. Dasgupta, R., Hirschmann, M. M. & Smith, N. D. Water follows carbon: CO2 incites deep silicate melting and dehydration beneath mid-ocean ridges. *Geology* **35**, 135 (2007).
4. Klein, E. M. & Langmuir, C. H. Global correlations of ocean ridge basalt chemistry with axial depth and crustal thickness. *J. Geophys. Res.* **92**, 8089 (1987).
5. Langmuir, C. H., Klein, E. M. & Plank, T. Petrological Systematics of Mid-Ocean Ridge Basalts: Constraints on Melt Generation Beneath Ocean Ridges. in *Geophysical Monograph Series* (eds. Morgan, J. P., Blackman, D. K. & Sinton, J. M.) 183–280 (American Geophysical Union, 1992). doi:10.1029/GM071p0183.
6. Phipps Morgan, J. & Chen, Y. J. Dependence of ridge-axis morphology on magma supply and spreading rate. *Nature* **364**, 706–708 (1993).
7. Chen, W.-P. & Molnar, P. Focal depths of intracontinental and intraplate earthquakes

and their implications for the thermal and mechanical properties of the lithosphere. *J. Geophys. Res. Solid Earth* **88**, 4183–4214 (1983).

8. Mckenzie, D., Jackson, J. & Priestley, K. Thermal structure of oceanic and continental lithosphere. *Earth Planet. Sci. Lett.* **233**, 337–349 (2005).
9. Grevemeyer, I. *et al.* Constraining the maximum depth of brittle deformation at slow- and ultraslow-spreading ridges using microseismicity. *Geology* **47**, 1069–1073 (2019).
10. deMartin, B. J., Sohn, R. A., Pablo Canales, J. & Humphris, S. E. Kinematics and geometry of active detachment faulting beneath the Trans-Atlantic Geotraverse (TAG) hydrothermal field on the Mid-Atlantic Ridge. *Geology* **35**, 711–714 (2007).
11. Parnell-Turner, R. *et al.* Oceanic detachment faults generate compression in extension. *Geology* **45**, 923–926 (2017).
12. Schlindwein, V. & Schmid, F. Mid-ocean-ridge seismicity reveals extreme types of ocean lithosphere. *Nature* **535**, 276–279 (2016).
13. Kohli, A., Wolfson-Schwehr, M., Prigent, C. & Warren, J. M. Oceanic transform fault seismicity and slip mode influenced by seawater infiltration. *Nat. Geosci.* **14**, 606–611 (2021).
14. Yu, Z. *et al.* Semibrittle seismic deformation in high-temperature mantle mylonite shear zone along the Romanche transform fault. *Sci. Adv.* **7**, eabf3388 (2021).
15. DeMets, C., Gordon, R. G. & Argus, D. F. Geologically current plate motions. *Geophys. J. Int.* **181**, 1–80 (2010).
16. Maia, M. & Brunelli, D. The Eastern Romanche ridge-transform intersection (Equatorial Atlantic): slow spreading under extreme low mantle temperatures. Preliminary results of the SMARTIES cruise. in *EGU General Assembly Conference Abstracts* 10314 (2020). doi:10.5194/egusphere-egu2020-10314.
17. Bonatti, E. *et al.* Diffuse impact of the Mid-Atlantic Ridge with the Romanche transform: an ultracold ridge-transform intersection. *J. Geophys. Res. Solid Earth* **101**, 8043–8054 (1996).
18. Bonatti, E. *et al.* Steady-state creation of crust-free lithosphere at cold spots in mid-ocean ridges. *Geology* **29**, 979–982 (2001).
19. Ligi, M., Bonatti, E., Cipriani, A. & Ottolini, L. Water-rich basalts at mid-ocean-ridge cold

spots. *Nature* **434**, 66–69 (2005).

20. Wang, Z. & Singh, S. *Seismic evidence for uniform crustal accretion along slow-spreading ridges in the equatorial Atlantic Ocean*. https://www.researchsquare.com/article/rs-1366304/v1 (2022) doi:10.21203/rs.3.rs-1366304/v1.
21. Cannat, M. *et al.* Modes of seafloor generation at a melt-poor ultraslow-spreading ridge. *Geology* **34**, 605–608 (2006).
22. Müller, R. D., Sdrolias, M., Gaina, C. & Roest, W. R. Age, spreading rates, and spreading asymmetry of the world's ocean crust. *Geochem. Geophys. Geosystems* **9**, Q04006 (2008).
23. Qin, Y., Singh, S. C., Grevemeyer, I., Marjanović, M. & Roger Buck, W. Discovery of flat seismic reflections in the mantle beneath the young Juan de Fuca Plate. *Nat. Commun.* **11**, 4122 (2020).
24. Molnar, P. The Brittle-Plastic Transition, Earthquakes, Temperatures, and Strain Rates. *J. Geophys. Res. Solid Earth* **125**, e2019JB019335 (2020).
25. Key, J., White, R. S., Soosalu, H. & Jakobsdóttir, S. S. Multiple melt injection along a spreading segment at Askja, Iceland. *Geophys. Res. Lett.* **38**, L05301 (2011).
26. White, R. S., Edmonds, M., Maclennan, J., Greenfield, T. & Agustsdottir, T. Melt movement through the Icelandic crust. *Philos. Trans. R. Soc. Math. Phys. Eng. Sci.* **377**, 20180010 (2019).
27. Wright, T. J. *et al.* Geophysical constraints on the dynamics of spreading centres from rifting episodes on land. *Nat. Geosci.* **5**, 242–250 (2012).
28. Feuillet, N. *et al.* Birth of a large volcanic edifice offshore Mayotte via lithosphere-scale dyke intrusion. *Nat. Geosci.* **14**, 787–795 (2021).
29. Martens, H. R. & White, R. S. Triggering of microearthquakes in Iceland by volatiles released from a dyke intrusion. *Geophys. J. Int.* **194**, 1738–1754 (2013).
30. White, R. S. *et al.* Dynamics of dyke intrusion in the mid-crust of Iceland. *Earth Planet. Sci. Lett.* **304**, 300–312 (2011).
31. Dixon, J. E., Stoper, E. M. & Holloway, J. R. An Experimental Study of Water and Carbon Dioxide Solubilities in Mid-Ocean Ridge Basaltic Liquids. Part I: Calibration and Solubility

Models. *J. Petrol.* **36**, 1607–1631 (1995).

32. Kisslinger, C. A review of theories of mechanisms of induced seismicity. *Eng. Geol.* **10**, 85–98 (1976).
33. Cartigny, P., Pineau, F., Aubaud, C. & Javoy, M. Towards a consistent mantle carbon flux estimate: Insights from volatile systematics (H_2O/Ce, δD, CO_2/Nb) in the North Atlantic mantle (14° N and 34° N). *Earth Planet. Sci. Lett.* **265**, 672–685 (2008).
34. Hauri, E. H. *et al.* CO_2 content beneath northern Iceland and the variability of mantle carbon. *Geology* **46**, 55–58 (2018).
35. Le Voyer, M. *et al.* Carbon Fluxes and Primary Magma CO_2 Contents Along the Global Mid-Ocean Ridge System. *Geochem. Geophys. Geosystems* **20**, 1387–1424 (2019).
36. Le Voyer, M., Kelley, K. A., Cottrell, E. & Hauri, E. H. Heterogeneity in mantle carbon content from CO2-undersaturated basalts. *Nat. Commun.* **8**, 14062 (2017).
37. Saal, A. E., Hauri, E. H., Langmuir, C. H. & Perfit, M. R. Vapour undersaturation in primitive mid-ocean-ridge basalt and the volatile content of Earth's upper mantle. *Nature* **419**, 451–455 (2002).
38. Kendrick, M. A. *et al.* Seawater cycled throughout Earth's mantle in partially serpentinized lithosphere. *Nat. Geosci.* **10**, 222–228 (2017).
39. Eguchi, J. & Dasgupta, R. A CO2 solubility model for silicate melts from fluid saturation to graphite or diamond saturation. *Chem. Geol.* **487**, 23–38 (2018).
40. Keller, T., Katz, R. F. & Hirschmann, M. M. Volatiles beneath mid-ocean ridges: Deep melting, channelised transport, focusing, and metasomatism. *Earth Planet. Sci. Lett.* **464**, 55–68 (2017).
41. Audhkhasi, P. & Singh, S. C. Discovery of distinct lithosphere-asthenosphere boundary and the Gutenberg discontinuity in the Atlantic Ocean. *Sci. Adv.* **8**, eabn5404 (2022).
42. Mehouachi, F. & Singh, S. C. Water-rich sublithospheric melt channel in the equatorial Atlantic Ocean. *Nat. Geosci.* **11**, 65–69 (2018).

Figures

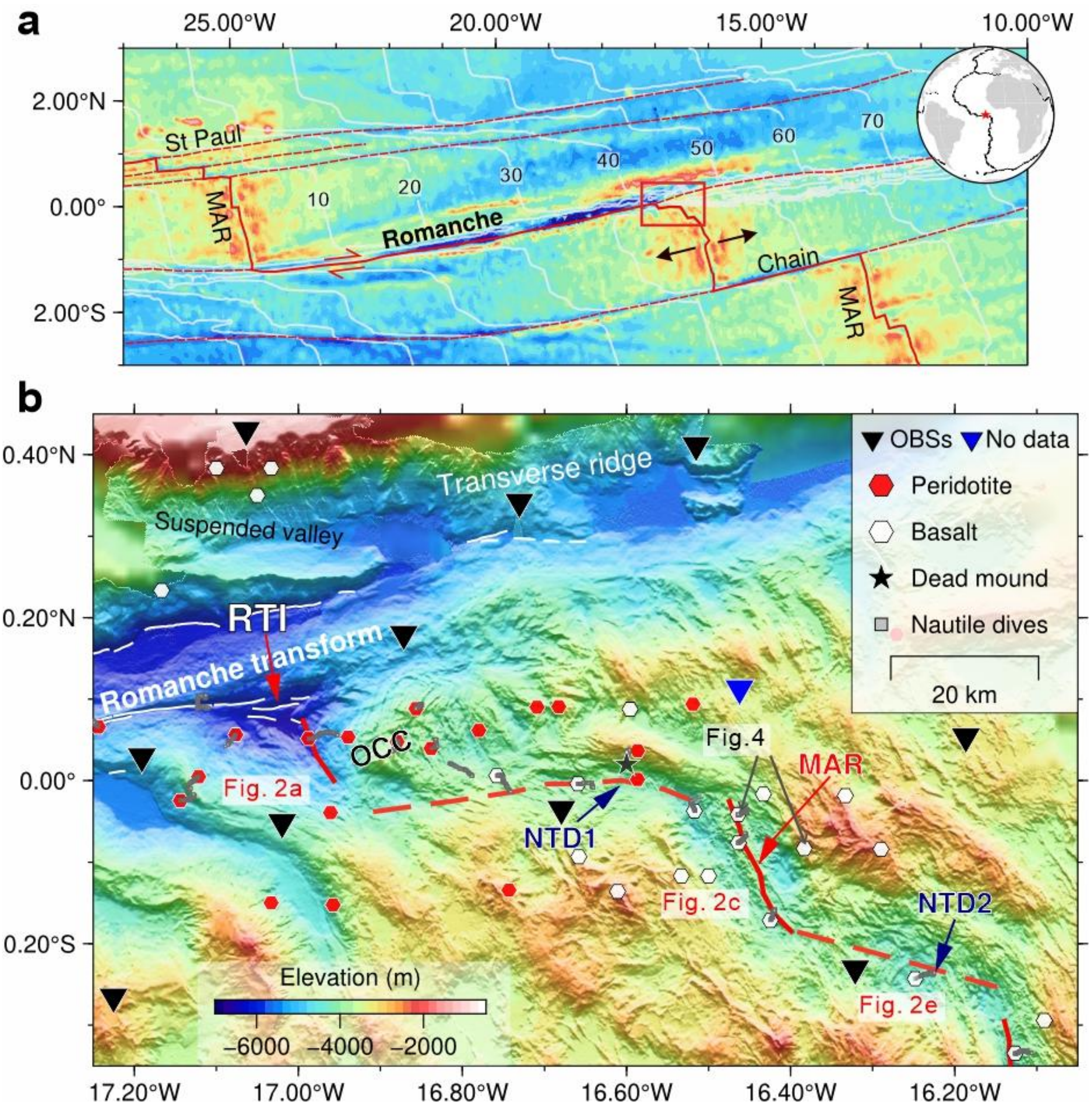

Fig. 1. Bathymetric map of the study area. (**a**) Major transform faults (solid red lines) and fracture zones (dashed red lines) in the equatorial Atlantic Ocean. The inset shows the location on a global map and the red rectangle marks the study area shown in (**b**). Thin gray lines indicate the lithospheric ages[22] every 10 Ma. MAR= Mid-Atlantic Ridge. (**b**) Bathymetric map with the location of rock samples in the vicinity of the eastern Romanche-MAR transform-ridge intersection (RTI), showing the area of the seismic experiment carried out during the SMARTIES cruise[16]. Solid and dashed red lines indicate the MAR axes and non-transform discontinuities (NTD) shown in Fig. 2, respectively. Rock samples are shown in colored hexagons[16,17] (see legend for symbols). The locations of rock samples used in Fig. 4 are marked. An

oceanic core complex (OCC) lies on the outside corner of the MAR. The triangles represent the deployed ocean-bottom seismometers (OBSs); the blue triangle indicates the OBS that did not generate seismic data. The black star indicates an inactive hydrothermal mound suggested by the Nautile dive observations (gray squares)[16]. The white lines show the faults along the Romanche transform. The color scale gives the water depth.

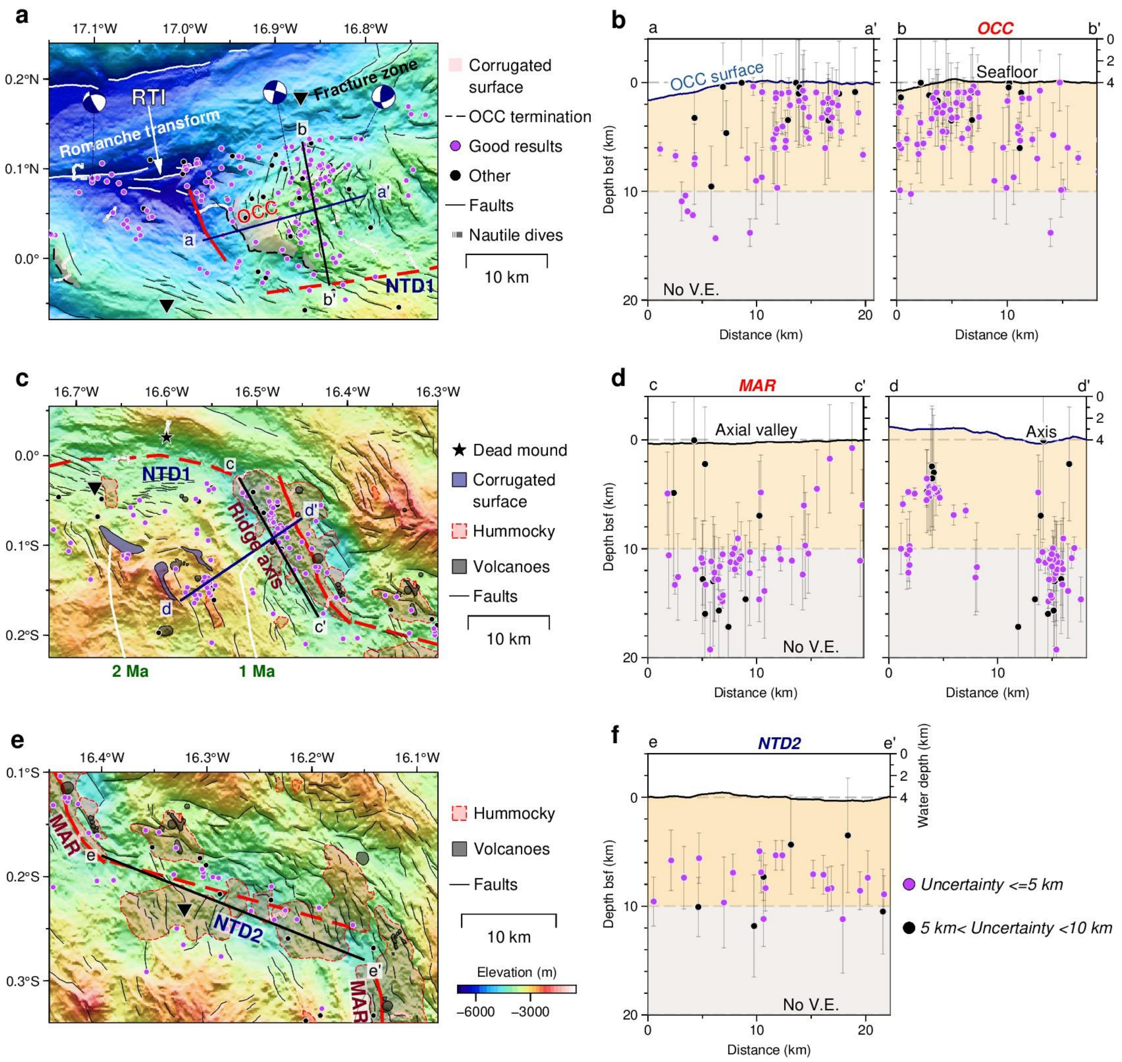

Fig. 2. Seismicity and tectonics at different segments. (**a**) Bathymetric map of the RTI area showing earthquakes and focal mechanisms. Tectonic information including the corrugated surface of the OCC, faults, transform fault trace, and termination of the OCC are marked (see legend for symbols). The earthquakes with uncertainties of ≤5 km are shown in magenta circles (uncertainties of 5-10 km in black). Blue and white beach balls indicate determined focal mechanisms. (**b**) Two transects of earthquake depth profiles, within ±5 km width of the profile, along and across the OCC marked by aa′ and bb′ in (**a**), respectively. The seafloor depth is marked on the upper part. Light brown areas indicate earthquake depths of <10 km and gray for event depths of >10 km. (**c**) Bathymetric map, events, and geological information along the MAR. Hummocky seafloor and volcanic cones are shown in red and gray shades,

respectively. The white lines indicate the lithospheric ages[22]. (**d**) Two transects of earthquake depths along (cc′) and across (dd′) the ridge axis. (**e**) Bathymetry, earthquakes, and geological information along the southern NTD (NTD2). (**f**) A transect of earthquake depth along the NTD2 (ee′). The other labeling is the same as that in Fig. 1b.

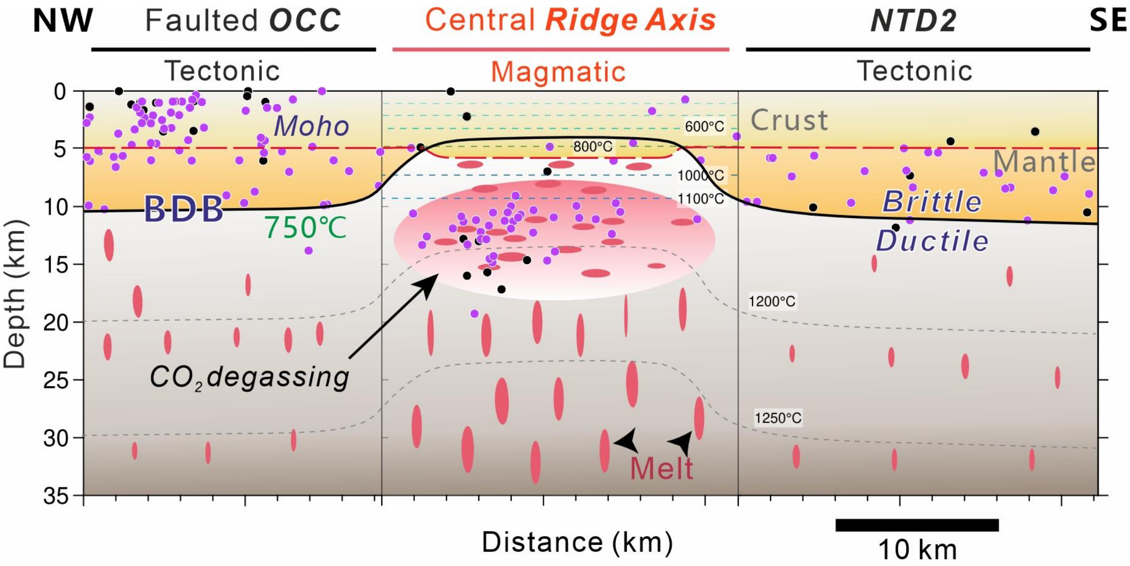

Fig. 3. Schematic diagram showing the seismicity along the MAR axis southward away from the Romanche transform fault. Three segments are illustrated. The brown and gray patches indicate the brittle and ductile lithosphere, respectively. The thick black line represents the BDB constrained by the maximum depth of earthquakes, corresponding to the 750 °C isotherm[6]. The crust beneath the central MAR segment is ~5.4±0.3 km thick[20], and the expected Moho interface is shown in a dashed red line. Deep earthquakes (10-19 km bsf) beneath the MAR axis, are interpreted as a result of volume change due to CO_2 degassing from the ascending melts in the hot ductile mantle. Colored dashed lines indicate the temperature isotherms extracted from a simulated thermal model[19].

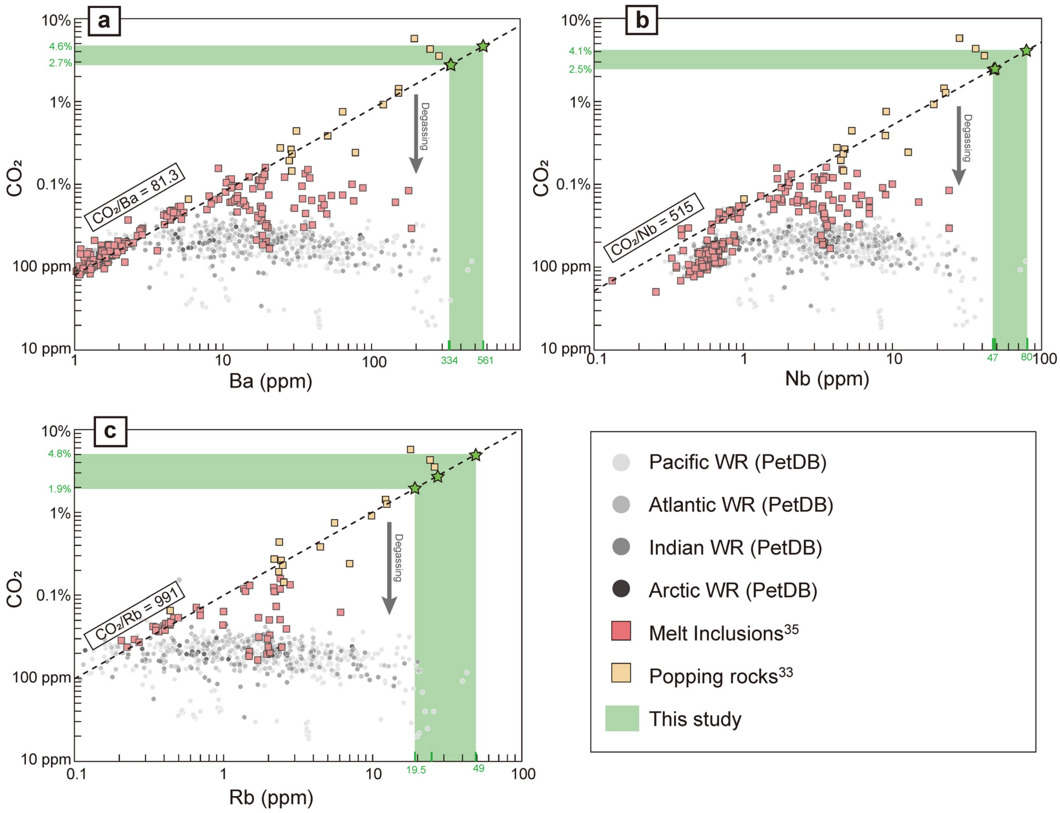

Fig. 4. CO_2 contents as a function of element composition. The CO_2 content as a function of Ba (**a**), Nb (**b**), and Rb (**c**) for MORB whole rocks (colored circles), melt inclusions (red squares)[35], popping rocks (yellow squares)[33], and the studied MORBs (green columns). The green stars indicate the estimated CO_2 contents on each map.

Methods

Seismic data

In July and August 2019, we conducted an ocean bottom seismometer (OBS) passive seismic experiment (Fig. 1b) during the SMARTIES cruise[43]. A network of 19 OBSs was deployed, covering the Romanche transform fault (TF) for ~140 km and the Mid-Atlantic Ridge (MAR) for ~120 km of their lengths, to record continuous seismicity data for ~21 days, with instrument spacing of ~30 km (Fig. 1b). We detected initial earthquake arrivals automatically using a short-term-average/long-term-average trigger algorithm within the SEISAN package[44] by analyzing the vertical components from 17 useful OBSs. In total, 760 earthquakes were detected and registered into a SEISAN database, each of which was detected by more than five arrivals and was then checked manually.

The reference one-dimensional (1-D) velocity model

The velocity structure of the study region is important for the precision of earthquake locations, and the closer it is to reality, the better earthquake locations will be. We constructed five 1-D P-wave velocity models (Extended Data Fig. 3a), derived from an active-source wide-angle seismic refraction profile[45], which provides velocity constraints at depths down to ~60 km below sea level. They include models beneath the northern flank, the transform valley, and the southern flank of the Romanche TF, a low-velocity model beneath the transform valley, and an average velocity model from north to south across the Romanche TF (Extended Data Fig. 3a). Then we used the five 1-D velocity models to locate earthquakes and selected the best one exhibiting the best possible combination of a large number of located events and a low average root mean square (RMS) residual (Extended Data Fig. 3b, Supplementary Table 2). As a result, the average velocity model was selected for the subsequent earthquake locations and focal mechanism computation (Extended Data Fig. 3b, Supplementary Table 2). Finally, 514 earthquakes were located (Extended Data Fig. 1), with depth uncertainties of ≤10 km, horizontal uncertainties of ≤10 km, RMS residuals of ≤0.3 s, and station gaps of <270°. Their mean horizontal and vertical errors are ~2.8 km and

~2.9 km, respectively (Supplementary Table 2). Wadati diagrams yield a Vp/Vs ratio of ~1.73 (Extended Data Fig. 4), which is used to estimate the S wave velocity in the inversion.

Earthquake location

We used the nonlinear oct-tree search algorithm of the NonLinLoc program[46] to locate initial earthquake hypocentres, of which the maximum likelihood solution was selected as the preferred result. NonLinLoc estimates a 3-D error ellipsoid (68% confidence) from the posterior density function scatter samples[46]. Iterative calculations of station corrections (Extended Data Fig. 5) were used to find the best solution as well as to remove the 3-D effects when the average RMS misfit yields a minimum (Extended Data Fig. 3b). At the same time, we removed the S-wave delays, which may be caused by the unconsolidated sediments[9], from the original S-onsets before the inversion[14].

After removing S-wave delays, double-difference relocations for 364 well-constrained events were determined using the hypoDD program[47]. All 364 earthquakes were detected on more than six OBSs, with RMS residuals of <0.25 s, uncertainties of <5 km, and azimuthal gaps of <270°. We performed the relocation using the differential travel times from the original catalog and waveform cross-correlation data. Station corrections (Extended Data Fig. 5) obtained by the NonLinLoc program were successfully applied. A minimum of 6 catalog links per event pair was required to form a continuous cluster. Five iterations were carried out, with a maximum event separation of 6 km. As a result, 276 events were well relocated, and they replaced the NonLinLoc locations in the final catalog. As a result, 317 events are located along the MAR and 197 events along the Romanche TF (Extended Data Fig. 1b), with an updated average horizontal uncertainty of ~2.1 km (Extended Data Fig. 1a).

Depth resolution

Earthquake depths along the MAR axis determined using five velocity models (Extended Data Fig. 3a) are shown in Extended Data Fig. 6. Our results show that most deep axial events are located between 10 and 20 km, whose depth shifts are smaller than the average depth uncertainties (~2.6 km) in all cases (Supplementary Table 2). However, the fastest model (Model 1), which is derived from the southern

Romanche TF[45], leads to some shallow events in the crust beneath the axial valley (Extended Data Fig. 6d). Notice that this model shows that the P-wave velocity exceeds 7.2 km/s at ~3 km depth, which is unusual for the MAR with crustal age of <7.5 Ma[48] (Extended Data Fig. 6b). Meanwhile, the southernmost flank bordering the Romanche TF is believed to be composed of mantle peridotites, representing a crust-free lithosphere (Fig. 1b)[14,16,18], therefore, this model is not reasonable for locating events beneath the MAR axis. We further examined the effect of velocity variations in ±0.1 km/s on the focal depths (Extended Data Fig. 7, Supplementary Table 3). Both the low- and high-velocity models can result in substantial deep events (>10 km) beneath the ridge axis (Extended Data Fig. 7c-e). Although the increased velocity model leads to some shallow events, it is also accompanied by a decrease in the number of located earthquakes (Supplementary Table 3). Meanwhile, the reduced velocity model leads to a smaller depth uncertainty (Extended Data Fig. 7c-e). Therefore, we believe that it is reasonable to use a normal- to low-velocity model in the study area rather than a fast velocity model. Almost all test models can produce deep events beneath the ridge axis (Extended Data Figs. 6-7), and therefore, we conclude their depths at 10-20 km are robust, not an artifact.

Magnitudes

Earthquake magnitudes were determined using the local magnitude scale M_L[49]: $M_L = lgA + 1.11\ lg\ (D) + 0.00189\ D - 2.09$. The maximum amplitude A is measured on a seismogram simulating the original Wood-Anderson seismogram using the SEISAN package[44]. D is the hypocentral distance in kilometers. The magnitude completeness (M_C, 1.5) and B-value (0.87) are also calculated using the ZMAP software[50] (Extended Data Fig. 8a). Earthquakes were divided into three groups, i.e., events along the TF, in the ridge-transform intersection (RTI), and along the MAR (Extended Data Fig. 8b-d). Their B-values were also determined, with small differences from each other (0.89-0.93) (Extended Data Fig. 8).

Focal mechanism solution

We used the P-phase first-motion polarities to determine focal mechanisms using the HASH package[51], and these polarities were picked from unfiltered earthquake waveform data on the vertical component. As previously noted[14], the obtained mechanism solutions are not very robust, mainly due to the large spacing of OBSs,

~30 km (Extended Data Fig. 1a). Also, the poor azimuthal ray path distribution limits the quality of the obtained results. Using a selection criterion based on P-wave polarities of >8, an azimuthal gap of <180°, an RMS fault plane uncertainty of <45°, average misfit <20%, station distribution ratio of >0.4, and mechanism probability >60% (Supplementary Table 4), we obtained 3 new well-constrained focal mechanisms (Extended Data Fig. 1a), together with three previous solutions for earthquake swarms[14] (Supplementary Table 4).

The maximum depth of earthquakes

We compiled the maximum depth of earthquakes along the ridge axis documented to date at slow- and ultraslow-spreading ridges around the world, as well as the full spreading rate on each site[15] (Extended Data Fig. 2, Supplementary Table 1). In this study, the selected maximum depth should be constrained by several earthquakes instead of only one event to avoid bias in the location process (Supplementary Table 1). Also, we included the information that may influence the maximum depth distribution, such as the development of oceanic core complexes and/or detachment faults, hydrothermal vents, magmatism (e.g., the focused melting and/or hotspots), and adjacent TFs (Extended Data Fig. 2, Supplementary Table 1). It should be noted that the reported data on the SWIR segment 8, SWIR oblique Supersegment, and the Logachev Seamount of Knipovich Ridge from ref.[12] were replaced with the newly located dataset[9,52,53]. Rainbow massif is located at the non-transform discontinuity (Supplementary Table 1), which was also included in the plot for reference (Extended Data Fig. 2).

CO_2 estimation from mid-ocean ridge basalts (MORB)

We analyzed two MORB samples along the studied MAR axis (0.04°S,16.46°W) collected by the Nautile dives during the SMARTIES cruise[43] (Fig. 1b). The two samples are SMA1974-278 collected at 3888 m below sea level (bsl), and SMA1974-279 at 3838 m bsl. We used the HR-ICP-MS Element XR - ThermoScientific (Pôle Spectrométrie Océan, Brest) for the trace elements analysis (Ba, Nb, and Rb). We also used one published MORB sample (No. 13-12 49A) along the present MAR axis (0.08°S,16.38°W)[38] (Supplementary Table 5).

The MORBs measured in this study contain Ba 329.96-334.21 ppm, Nb 46.94-48.48 ppm, and Rb 19.52-25.27 ppm (Fig. 4, Supplementary Table 5). The CO_2/Ba ratios of melt inclusion from the MORBs are believed to be a good proxy for the CO_2 concentration[34–37]. If we use a constant CO_2/Ba ratio (81.3 ± 23)[35], the estimated CO_2 concentration in the undegassed mantle melt would be ~2.7-4.6 wt% (Fig. 4a). Using a constant CO_2/Nb ratio (515 ± 112)[33] (Fig. 4b), the estimated CO_2 content is ~2.5-4.1 wt%. Using a constant CO_2/Rb ratio (991 ± 129)[35] (Fig. 4c), the estimated CO_2 content is ~1.9-4.8 wt%. These results suggest that the CO_2 concentration from the three samples is at least >1.9 wt%.

CO_2 estimation from seismicity

Mantle earthquakes (depth >10 km) beneath the ridge axis show an average local magnitude (M_L) of ~1.7 for 34 events, all of which are not greater than M_L 2.8 (Extended Data Fig. 9). For small events, the moment magnitude (M_w) is assumed to be equal to the local magnitude[54]. If the deep mantle earthquakes are due to the CO_2 degassing, we assume that the subsequent volume change is equivalent to the fault size. Using the scale relationship between rupture fault size and moment magnitude[55,56] (Extended Data Fig. 10), the rupture width of these axial mantle events is ~50-200 m when stress drop ranges from 0.1 MPa to 10 MPa following the circular source theory[56] (Extended Data Fig. 10). In this case, the estimated average fault length would be ~100 m, and the greatest length would be <1 km (Extended Data Fig. 10). The seismogenic zone of deep mantle earthquakes is ~13 km long (between 2 and 15 km distance in Fig. 2d) and 6 km wide (focal depths of 10-16 km) (Fig. 3), resulting in a surface of ~78 km^2. Using the magnitude-fault scale relationship[55,56] (Extended Data Fig. 10), the total maximum area of the rupture region for ~40 small events at depths of 10-16 km can reach $40 \times 200\ m \times 200\ m = 1.6\ \text{km}^2$, equivalent to ~2.1% of volume change in the deep seismogenic zone resulting from the CO_2 degassing. Apparently, this value is overestimated as many earthquakes can originate in the same volume space. If we use the average fault length (~100 m), the estimated average amount of volume change by CO_2 degassing would be ~0.5%.

Data and materials availability:

Raw seismic data and cruise reports can be requested from the website (https://campagnes.flotteoceanographique.fr/campagnes/18001107/). The earthquake catalog and picked P- and S-arrivals will be available on the Zenodo dataset repository upon the acceptance of the manuscript.

Code availability

The SEISAN software[44] used to pick phases is available at https://www.geo.uib.no/seismo/SOFTWARE/SEISAN/. The NonLinLoc code[46] used for earthquake location is available at http://alomax.free.fr/nlloc/. The HypoDD program (version 1.3)[47] used for double-difference earthquake relocation is available at https://www.ldeo.columbia.edu/~felixw/hypoDD.html. The ZMAP software[50] used for catalog analysis to obtain B-value and magnitude completeness is available at https://github.com/swiss-seismological-service/zmap7. The HASH software[51] (version 1.2) used for determining focal mechanisms solution is available at https://www.usgs.gov/node/279393. The Global Mapper used for structural analysis is available at https://www.bluemarblegeo.com/global-mapper/. The GMT 6 toolbox[57] used for graphing is available at https://www.generic-mapping-tools.org/download/.

References

43. Maia, M., Brunelli, D. & Ligi, M. SMARTIES cruise,Pourquoi pas? R/V. (2019) doi:10.17600/18001107.

44. Havskov, J. & Ottemoller, L. SEISAN earthquake analysis software. *Seismol. Res. Lett.* **70**, 532–534 (1999).

45. Wang, Z., Singh, S., Prigent, C., Gregory, E. & Marjanovic, M. *Lithospheric thinning due to hydration and melting at oceanic transform plate boundaries.* https://www.researchsquare.com/article/rs-255780/v1 (2021) doi:10.21203/rs.3.rs-255780/v1.

46. Lomax, A., Virieux, J., Volant, P. & Berge-Thierry, C. Probabilistic earthquake location in 3D and layered models. in *Advances in seismic event location* 101–134 (Springer, 2000).

47. Waldhauser, F. & Ellsworth, W. L. A double-difference earthquake location algorithm: Method and application to the northern Hayward fault, California. *Bull. Seismol. Soc. Am.* **90**, 1353–1368 (2000).

48. Christeson, G. L., Goff, J. A. & Reece, R. S. Synthesis of Oceanic Crustal Structure From Two-Dimensional Seismic Profiles. *Rev. Geophys.* **57**, 504–529 (2019).
49. Hutton, L. & Boore, D. M. The ML scale in southern California. *Bull. Seismol. Soc. Am.* **77**, 2074–2094 (1987).
50. Wiemer, S. A Software Package to Analyze Seismicity: ZMAP. *Seismol. Res. Lett.* **72**, 373–382 (2001).
51. Hardebeck, J. L. & Shearer, P. M. A new method for determining first-motion focal mechanisms. *Bull. Seismol. Soc. Am.* **92**, 2264–2276 (2002).
52. Aupart, C., Schlindwein, V., Ben-Zion, Y., Renard, F. & Jamtveit, B. *Seismic controls on the progress of serpentinization at ultra-slow spreading ridges.* http://www.essoar.org/doi/10.1002/essoar.10502242.1 (2020).
53. Meier, M. *et al.* Segment-Scale Seismicity of the Ultraslow Spreading Knipovich Ridge. *Geochem. Geophys. Geosystems* **22**, e2020GC009375 (2021).
54. Kuna, V. M., Nábělek, J. L. & Braunmiller, J. Mode of slip and crust–mantle interaction at oceanic transform faults. *Nat. Geosci.* **12**, 138–142 (2019).
55. Zoback, M. D. & Gorelick, S. M. Earthquake triggering and large-scale geologic storage of carbon dioxide. *Proc. Natl. Acad. Sci.* **109**, 10164–10168 (2012).
56. Scholz, C. H. *The Mechanics of Earthquakes and Faulting*. (Cambridge University Press, 2019). doi:10.1017/9781316681473.
57. Wessel, P. *et al.* The Generic Mapping Tools Version 6. *Geochem. Geophys. Geosystems* **20**, 5556–5564 (2019).
58. Hicks, S. P. *et al.* Back-propagating supershear rupture in the 2016 M_w 7.1 Romanche transform fault earthquake. *Nat. Geosci.* **13**, 647–653 (2020).
59. Chatelain, J. L. Etude fine de la sismicité en zone de collision continentale au moyen d'un réseau de stations portables: la région Hindu-Kush Pamir. (Université scientifique et médicale de Grenoble, 1978).

Acknowledgments

We are grateful to the officers, crew, and scientific technicians for their hard work during the 2019 SMARTIES cruise. We thank P. Cartigny and L. Geli for the useful discussions. **Funding:** This research was funded by the ISblue project, Interdisciplinary graduate school for the blue planet (ANR-17-EURE-0015), the French government under the program "Investissements d'Avenir", the Regional Council of Brittany (SAD programme), the European Research Council under the European Union's Seventh Framework Programme (FP7/2007–2013), and the ERC Advanced Grant agreement no. 339442_TransAtlanticILAB. The ship time for the SMARTIES cruise was funded through the TGIR French Oceanographic Fleet.

Author Contributions

Z.Y. processed the seismicity data, analyzed the results, and wrote the paper. S.C.S. supervised the data acquisition, data processing, and interpretation of the seismic data, developed the idea, and wrote the paper. L.G. performed the geochemical measurements. C.H. performed elemental analysis and interpretation. M.M., A.B., and L.P. performed the structural analysis. M.M. and D.B. designed the SMARTIES project. M.M., D.B., A.B., and L.P. participated in the data collection during the SMARTIES cruise. All authors discussed the results and commented on the manuscript.

Competing interests

The authors declare no competing interests.

Additional information

Supplementary information is available for this paper. Correspondence and requests for materials should be addressed to Zhiteng Yu. Reprints and permissions information is available at www.nature.com/reprints.

Extended Data legends

Extended Data Fig. 1

Seismicity. (**a**) Bathymetric map with seismicity in the study region, whose location is shown in the inset map on the upper left corner, in which white lines indicate the lithospheric ages[22] every 10 Ma. Solid and dashed red lines indicate the Mid-Atlantic Ridge (MAR) axes and non-transform discontinuities (NTD) shown in Fig. 2, respectively. Focal mechanisms (Supplementary Table 4) are shown in blue and white beach balls. Rock samples are shown in colored hexagons[16–18], and the average horizontal uncertainty (~2.1 km) after the relocation is marked by a black plus sign (see legend for symbols). The red star with a beach ball and two blue stars indicate the 2016 M_w 7.1 Romanche earthquake and two subevents, respectively[58]. The dashed red line shows the seismic refraction profile[45]. (**b**) Earthquake depths along the Romanche transform fault (TF) (white line in **a**) and along the MAR (red line in **a**) within ±10 km width of the profile. The bottom histograms show the numbers of earthquakes along the profile. Zero position is the ridge-transform intersection (RTI) location. The white circle and red squares on the top mark the 20 km intervals and longitudes for reference. Depth uncertainties are plotted in gray lines. The other labeling is the same as that in Fig. 1.

Extended Data Fig. 2

Statistics for the maximum depth distribution of seismicity and full spreading rates. Depths of earthquakes for slow- and ultraslow-spreading ridges are shown in blue and brown circles, respectively, whose locations are shown on the inset map. The color scale gives full spreading rates. The dashed black line indicates the 750℃ isotherm[6]. The maximum depths are affected by several processes, e.g., detachments faults (triangles), hydrothermal vents (diamonds, a black one is inactive), volcanoes/hotspots (squares), and TFs (hexagons) (see legend for symbols). A compilation of all the depth data and references used in this figure can be found in Supplementary Table 1.

Extended Data Fig. 3

1-D P-wave velocity models. (**a**) Five 1-D models are derived from an active-source wide-angle seismic refraction profile[45]. The gray shade represents the velocity of the crust with age <7.5 Ma[48]. (**b**) Average RMS residuals (dashed lines with circles) and the number of located earthquakes (solid lines with inverted triangles) as a function of iterations using the five 1-D models shown in (**a**). The vertical green bar indicates the selected results for each 1-D velocity model. Model 5 (magenta) is the selected model for the earthquake location (see Supplementary Table 2).

Extended Data Fig. 4

Wadati diagrams. (**a**) Original computation showing P-onset versus S-P time. (**b**) A modified computation showing time differences between P-arrivals (Pi-Pj) versus those between S-arrivals (Si-Sj) for each station pair (i, j) of each event[59]. In this study, the Vp/Vs ratio is ~1.73, which is used to estimate the S-wave velocity for the earthquake location.

Extended Data Fig. 5

Cumulative travel time residuals. Average residuals for P- (**a**) and S-arrivals (**b**) on each station using the NonLinLoc location program[46]. Triangles indicate the locations of ocean bottom seismometers used in this study. The red line shows the location of the seismic refraction profile[45].

Extended Data Fig. 6

Earthquake depths along the MAR with five different 1-D velocity models. (**a**) Bathymetric map and located events. Solid and open dots indicate earthquakes with depth uncertainty of ≤5 km and 5-10 km, respectively. The color gives the results using different velocity models in (**b**). One transect along the ridge axis is shown in (**c, d**). The black star indicates an inactive hydrothermal mound suggested by the dive observations[16]. (**b**) Five tested 1-D velocity models. (**c-d**) The focal depth distribution of earthquakes along the profile (aa′) in (**a**). Gray lines mark the depth uncertainties. The histograms on the right show the depth distributions for the different 1-D velocity models in (**b**). A short column with a number is plotted for reference. Velocity Model

1 is too fast and not reasonable (see Methods). The other labeling is the same as that in Extended Data Fig. 1.

Extended Data Fig. 7

Depth resolution test along the MAR with three different 1-D velocity models. (**a**) Bathymetric map and located events. (**b**) A reduced velocity model by -0.1 km/s (red), an increased velocity model by +0.1 km/s (blue), and the final velocity model (black) are constructed. (**c-d**) The focal depth distribution of earthquakes along the profile (aa′) in (**a**). The other labeling is the same as that in Extended Data Fig. 6.

Extended Data Fig. 8

Histograms of local magnitudes (M_L). Earthquakes in the full catalog (**a**), along the Romanche TF (**b**), in the RTI (**c**), and along the MAR (**d**) are shown in gray, red, green, and blue columns, respectively. The cumulative number of events is marked by blue squares on each map. Catalogs are analyzed using the ZMAP software[50] to obtain the magnitude completeness (M_C) and B-values.

Extended Data Fig. 9

Seismicity, tectonic information, earthquake temporal distribution along the MAR. (**a**) Bathymetric map, events, and geological information. Hummocky seafloor and volcanic cones are shown in red and gray shades, respectively. One transect along the ridge axis is shown in (**b**). Triangles mark the deployed OBSs. (**b**) The cross-section of earthquakes. (**c**) The focal depth distribution of earthquakes as a function of dates from 19 July to 16 August 2019. Magnitude scales are shown on the top.

Extended Data Fig. 10

Scale relationships between fault length and magnitude were modified from Ref.[55,56]. Three thick lines indicate stress drops ranging from 0.1 MPa to 10 MPa. In this study, the averaged magnitude (M_L ~1.7) of the axial mantle earthquakes (Extended Data Fig. 9) is shown in dashed blue lines, assuming moment magnitude

M_w=M_L for small events[54], leading to the fault size ranging between 50 m and 200 m. The dashed red lines indicate the fault sizes for the maximum M_w of 2.8.

Supplementary Files

This is a list of supplementary files associated with this preprint. Click to download.

- Supplementaryfinal.pdf
- ExtendedData.pdf